Available online at www.sciencedirect.com
ScienceDirect
Journal of Sound and Vibration 322 (2009) 1081–1099
JOURNAL OF SOUND AND VIBRATION
www.elsevier.com/locate/jsvi

Vibration analysis of vector piezoresponse force microscopy with coupled flexural-longitudinal and lateral-torsional motions

Amin Salehi-Khojin, Nader Jalili*, S. Nima Mahmoodi

Smart Structures and Nanoelectromechanical Systems Laboratory, Department of Mechanical Engineering, Clemson University, Clemson, SC 29634-0921, USA

Received 2 May 2008; received in revised form 11 November 2008; accepted 25 November 2008
Handling Editor: C.L. Morfey
Available online 14 January 2009

Abstract

Piezoresponse force microscopy (PFM) has evolved into a useful tool for measurement of local properties of piezoelectric materials with great potential in applications such as data storage, ferroelectric lithography and nonvolatile memories. In order to utilize PFM for low dimensional materials characterization, a comprehensive analytical modeling based on the coupled motion of PFM in all three directions is proposed. In this respect, the mechanical properties of sample are divided into viscoelastic and piezoelectric parts. The viscoelastic part is modeled as a spring and damper in the longitudinal, transversal and lateral directions, while the piezoelectric part is replaced with resistive forces acting at the end of microcantilever. It is shown that there is a geometrical coupling between flexural-longitudinal and lateral-torsional vibrations of microcantilever used in PFM. Moreover, assuming a general friction between tip and sample, additional coupling effect is also taken into account. Through an energy-based approach, it is seen that the PFM system can be governed by a set of coupled partial differential equations along with nonhomogeneous and coupled boundary conditions. A general formulation is then derived for the mode shape, frequency response, and state-space representation of system. Numerical simulations indicate that mode shapes, natural frequencies and time responses of microcantilever beam are heavily dependent on the viscoelastic and piezoelectric properties of the samples. Moreover, the results demonstrate that utilizing only transversal vibration is not a valid strategy for quantifying mechanical properties of materials with arbitrary crystallographic orientation. Hence, the proposed model with the built-in coupling effects can be a key development for acquiring precise measurements.

1. Introduction

In recent years, rapid development in scanning probe microscopy-based techniques has made it possible to study properties of materials in the scale of grains. Among the many scanning probe microscopy techniques, atomic force acoustic microscopy and piezoresponse force microscopy (PFM) have evolved into useful tools for this purpose due to their ease of implementation and high resolution [1–8]. The operational principle of atomic force acoustic microscopy is based on measuring the contact stiffness of the tip-sample junction as the result of the change in the dynamic properties of microcantilever. In this technique, the sample is vibrated by

*Corresponding author. Tel.: +1 864 656 5642; fax: +1 864 656 4435.
E-mail address: jalili@clemson.edu (N. Jalili).

0022-460X/$ - see front matter © 2008 Elsevier Ltd. All rights reserved.
doi:10.1016/j.jsv.2008.11.039

ultrasonic transducer on the resonant frequencies of cantilever and through measuring contact resonant spectra, the contact stiffness of material can be determined [8]. While the atomic force acoustic microscopy allow us to probe the tip-sample interaction force such as stiffness and adhesion, PFM enables investigation of local piezoelectricity of material as well. For this reason, this technique has been recognized as a useful tool in the field of micro- and nano-scale electromechanical sensors and actuators [9–11].

PFM functions based on applying an external electrical field between a rear electrode on the piezoelectric sample and a conducting atomic force microscopy tip. In the static mode, application of uniform electric field results in elongation or contraction of sample depending on the polar direction and applied field. From induced strain through electric field, the piezoelectric coefficient of sample can be determined. However, the domain imaging based on the detection of static deformation is difficult. The reason is that the separation of static piezoresponse deflection and deflection signal due to surface roughness is not an easy task [12]. To improve the sensitivity of the static mode, a dynamic piezoresponse image method based on the voltage modulation approach has been introduced [12–15]. In this method, a periodic bias external electrical field is applied to a rear electrode on the sample and a conducting tip. The periodic bias voltage induces local piezoelectric vibration which can be detected by tip. These vibrations depend on the orientation of polarization vector, and arise due to converse piezoelectric effect [16]. The phase of electromechanical response of surface provides information about the direction of polarization of surface, while the amplitude of vibration yields information about the piezoelectric coefficients [17,18].

In general case, when a bias voltage is applied to a sample with arbitrary crystallographic orientation, the response of the piezoelectric material results in both in-plane and normal components of displacement [19]. Hence, the microcantilever can vibrate in all three directions which results in a coupled bending–longitudinal-torsional motion of microcantilever. The coupled motions in PFM occur due to: (i) presence of friction force at the tip-sample junction and (ii) geometrical coupling originated from the rotation of tip at the free end of microcantilever due to transversal and lateral bending of microcantilever.

Because of practical importance of coupled motions, many studies have been reported on the effect of coupling terms on the natural frequencies, mode shapes and time responses of the beams [20–24]. Neglecting the effect of warping, Dokumaci [25] obtained the natural frequencies of a cantilever coupled in bending and torsion. His work was later extended by Bishop et al. [26] including the wrapping of cross section. A dynamic stiffness matrix analysis approach was then introduced by Banerjee et al. [27] to determine the natural frequencies and mode shapes of the coupled Euler–Bernoulli beam. The coupled vibrations of beams including warping, shear deformation and rotary inertia effects were studied by Bercin and Tanaka [28]. The coupled free and forced vibrations of a beam with tip and in-span attachments were investigated by Gokdag and Kopmaz [29]. And recently, Mahmoodi and Jalili have investigated the nonlinear flexural–torsional coupled vibration of microcantilever sensors [30]. The results obtained from these studies have addressed the presence of bending, longitudinal or torsional mode natural frequency in the vibration spectra of the other modes.

Motivated by these considerations, the objective of this study is to develop a comprehensive model for dynamic behavior of vector PFM system under applied combined electrical and mechanical loadings. For this purpose, PFM is considered as a suspended microcantilever beam with a tip mass in contact with a piezoelectric material. Furthermore, the material properties are expressed in two forms; Kelvin–Voigt model for viscoelastic representation of material and piezoelectric force acting on the tip as a result of response of material to applied electric field. Since the application of bias voltage to the tip results in the surface displacement in both normal and in-plane directions [31], the microcantilever is considered to vibrate in all three directions with coupled flexural-longitudinal and lateral-torsional motions. In this model, the effect of friction between sample and tip is also taken into account.

Through an energy-based approach, it is shown that the PFM system can be governed by a set of coupled partial differential equations along with nonhomogeneous and coupled boundary conditions. A general formulation is then derived for the mode shape and frequency response of the system. Finally, using the method of assumed modes, the governing ordinary differential equations of the system and its state-space representation are derived under applied external voltage. Results demonstrate that mode shape, resonance frequency and time response of microcantilever are heavily dependent on the coupling terms arising from viscoelastic and piezoelectric properties of samples. It is shown that different materials exhibit various constraints at the end of microcantilever. More specifically, materials with higher stiffness can convert the

clamped-free condition of microcantilever to clamped-hinged one. Moreover, it is shown that the coupled damping terms of material at the tip-sample junction significantly affect the time response of the system. The modeling framework presented in this work can also be easily reduced to atomic force acoustic microscopy problem.

2. PFM operational modes and function

PFM functions based on application of a periodic bias external electrical field between a rear electrode on the sample and a conducting tip (see Fig. 1). The periodic bias voltage is $V_{tip} = V_{dc} + V_{ac}\cos(wt)$ in which V_{dc} is the DC component of the bias voltage used to measure the static deflection of the microcantilever. $V_{ac}\cos(wt)$ is a small AC voltage which is applied to the tip in order to induce local piezoelectric vibration. The piezoresponse of the surface can be detected as the first harmonic component of bias-induced tip deflection $d = d_0 + A\cos(wt + \varphi)$. The amplitude of vibration, A, provides information about the piezoelectric coefficients of surface, while the phase of electromechanical response of surface, φ, yields information about the polarization direction of surface [4,17].

Utilizing Hertzian contact mechanics at the tip-sample junction and assuming linear voltage dependency of indentation [4,31], the relation between the indentation load P, indenter voltage V, and indentation depth h can be expressed as [31]

$$h = \frac{a^2}{R} + \frac{2\beta}{3\alpha}V \quad \text{and} \quad P = \alpha\frac{a^3}{R} - \beta a V, \tag{1}$$

where α and β are elastic and piezoelectric properties of material, respectively, R is the tip radius and a is the contact radius. In this study, based on Eq. (1), the behavior of sample is divided into two parts; viscoelastic and piezoelectric. The viscoelastic response of material against indentation force is modeled as a spring and damper at all three directions, while the piezoresponse of sample is considered as a resistance force, F_{tip}, at the free end of cantilever.

Fig. 2 depicts the schematic of mechanical equivalent circuit of PFM. One end of the beam is clamped to the base position, while the tip is attached to the free end of the beam. The sample and tip are in the contact mode and any change in the topography of surface will affect the indentation depth of indenter. To avoid this, the boundary control input force, $f(t)$, is used at the base unit. In general case, when a bias voltage is applied to a

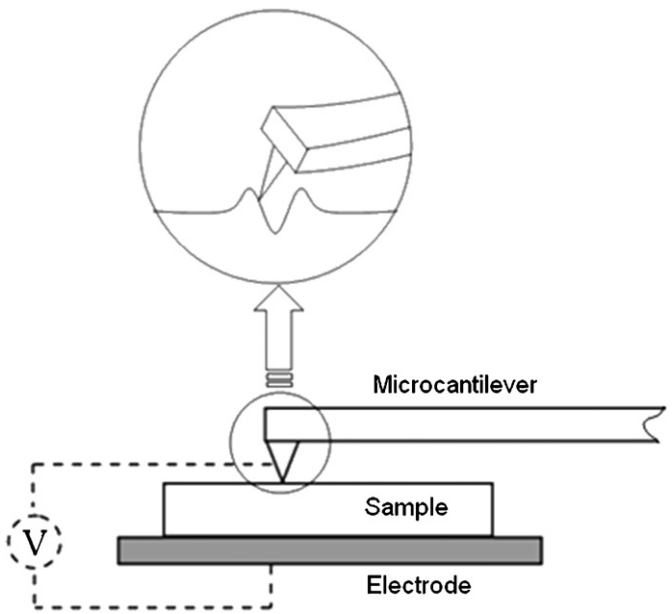

Fig. 1. A schematic of tip-sample junction in piezoresponse force microscopy.

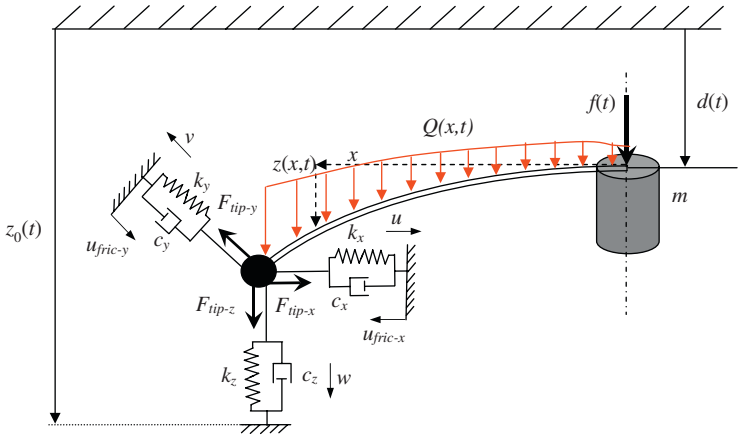

Fig. 2. Proposed schematic representation of piezoresponse force microscopy.

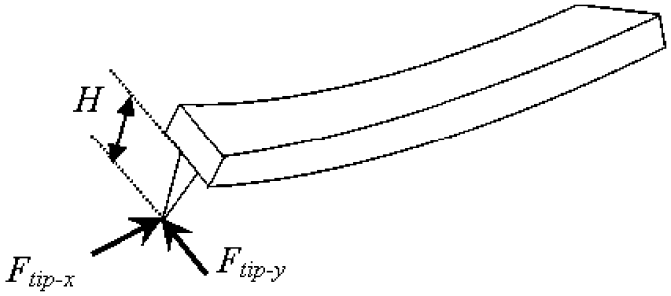

Fig. 3. A schematic of microcantilever subjected to longitudinal and lateral piezoelectric forces.

sample with arbitrary crystallographic orientation, the response of the piezoelectric material results in both in-plane and normal components of displacement [19]. For this reason, the beam is considered to vibrate in all three directions. The free end of beam with the equivalent tip mass is connected to springs and dampers in the vertical, longitudinal and lateral directions which represent the viscoelastic resistance of material to tip movement. It is obvious that lateral and vertical components of viscoelastic response acting on the cantilever result in bending in these directions, while in the longitudinal direction the response of material is an axial force acting at the tip mass. Moreover, the piezoresponse of material is considered as F_{tip} in all three directions (i.e., $F_{\text{tip-}x}$, $F_{\text{tip-}y}$ and $F_{\text{tip-}z}$). In our proposed model, the tip height is also taken into account. As a result, piezoresponse of material acting at the end of tip causes an external moment and torsion in the longitudinal and lateral directions, respectively. Fig. 3 depicts longitudinal and lateral piezoelectric forces acting at the tip of microcantilever.

In this study, the effect of friction force presented in the tip-sample junction in both longitudinal and lateral directions are considered as base excitations given by

$$u_{\text{fric-}x} = \Delta x = \frac{\mu_x F_{\text{tip-}z}}{k_x} \quad \text{and} \quad u_{\text{fric-}y} = \Delta y = \frac{\mu_y F_{\text{tip-}z}}{k_y}, \quad k_x = k_y \neq 0, \tag{2}$$

where μ_x and μ_y are the coefficients of friction in x and y directions, respectively. Eq. (2) indicates that the friction force in PFM system is a time-dependent parameter.

3. Distributed-parameters modeling of PFM

In this section, a general distributed-parameters base modeling approach is adopted for the analysis of dynamic behavior of PFM. For this purpose, the Euler–Bernoulli model is used for microcantilever beam

configuration as shown in Fig. 2. The microcantilever beam has rigidity EI, mass moment of inertia J, linear density ρ and the length L. The equivalent spring constants of sample are k_x, k_y and k_z, and damping coefficients are C_x, C_y and C_z in x, y, z directions, respectively. The microcantilever base has the displacement of $d(t)$ and the total mass of m, while the tip at the free end of beam has mass of m_e. The friction coefficients between sample and tip are μ_x and μ_y for in-plane motions. In this work, the effect of viscous air damping and structural damping in the microcantilever beam are also taken into account.

The total kinetic energy of the system can now be expressed as

$$\mathrm{KE} = \frac{1}{2}m(\dot{d}(t))^2 + \frac{1}{2}\int_0^L \rho[(\dot{d}(t) + w_t(x,t))^2 + v_t^2(x,t) + u_t^2(x,t)]\,\mathrm{d}x + \frac{1}{2}m_e[(\dot{d}(t) + w_t(L,t))^2 + v_t^2(L,t) + u_t^2(L,t)] + \frac{1}{2}\int_0^L J\theta_t^2(x,t)\,\mathrm{d}x, \tag{3}$$

where subscripts $(\cdot)_t$ and $(\cdot)_x$ indicate partial derivatives with respect to the time variable t and position variable x, respectively. $w(x,t)$, $u(x,t)$ and $v(x,t)$ are the vertical, longitudinal and lateral displacements of beam, respectively. $\theta(x,t)$ represents the torsion along x-axis due to applied voltage and friction. In the above equation, the first term is the kinetic energy of the base, the second and third terms are that of beam and tip, respectively. The last term represents the kinetic energy due to torsion of beam along x-axis.

The total potential energy of the system can be written as

$$\mathrm{PE} = \left\{\frac{1}{2}\int_0^L EI_{yy}w_{xx}^2(x,t)\,\mathrm{d}x + \frac{1}{2}\int_0^L EI_{zz}v_{xx}^2(x,t)\,\mathrm{d}x\right\} + \frac{1}{2}\int_0^L EAu_x^2(x,t)\,\mathrm{d}x + \frac{1}{2}\int_0^L C_T\theta_x^2(x,t)\,\mathrm{d}x + \left\{\frac{1}{2}k_x[(u(L,t) + u_{\text{fric-}x}) + w_x(L,t)H]^2 + \frac{1}{2}k_y[(v(L,t) + u_{\text{fric-}y}) - \theta H]^2 + \frac{1}{2}k_z w^2(L,t)\right\}, \tag{4}$$

where H is the height of tip at the free part of beam, and C_T is the torsional stiffness of beam. The above equation indicates that potential energy consists of four parts: the potential energy of the beam due to bending in vertical and lateral direction (first term), the potential energy of the beam due to longitudinal movement (second term), torsion along x-axis (third term), and the elastic potential energy of sample in the longitudinal, lateral and vertical directions, respectively (last term). In addition to tip displacement at the free end of microcantilever, the elastic potential of sample in the longitudinal and lateral directions include base excitation terms due to presence of friction and geometrical coupling due to rotation of tip as a result of transversal and lateral bending. In the above equation, $w_x(L,t)H$ presents the geometrical coupling term between transversal and longitudinal direction and θH indicates coupling between lateral bending and torsional displacement. In this model, the friction effect is implemented as a base excitation in the elastic potential energy of sample. The base displacement of sample is directly related to piezoelectric properties of material obtained in Eq. (2).

The boundary control input force $f(t)$ at the base unit, the piezoelectric force, capacitive forces between tip cantilever assembly and surface $Q(x,t)$, structural damping C, and viscous air damping B are all considered in the virtual work. While the viscous air damping B, which is the case for this work, can be fairly assumed as a frequency independent parameter, the viscous liquid damping is frequency dependent. It has been shown that at higher frequency, the volume of liquid excited by cantilever is reduced compared to lower frequencies vibration which results in reduced viscous damping in the higher resonances [32,33]. Moreover, the viscous liquid loss has been shown to significantly affect the resonance frequencies of microcantilever. In this respect, the effect of surrounding liquid on the dynamic properties of cantilever has been investigated by other researcher using added mass coefficient [34,35]. However, in the current case (viscous air damping) and for simplicity and without loss of generality, it is assumed that viscous air damping and structural damping coefficients in the transversal and lateral directions are similar.

Moreover, the piezoelectric and damping forces acting at the tip-sample junction are considered as an equivalent impulse (Δ) forces acting at very small distance (ε) from end of microcantilever. This approach can ease the subsequent mathematical procedures used to homogenize the boundary conditions. More especially, utilizing this approach the damping terms in the boundary conditions can be removed and transferred into the equations of motion. However, the conventional method is to consider damping terms in the boundary conditions which makes the nature of them time-dependent. In this case, the eigenvalues and subsequent mode

shapes of the system become complex, which are more complicated to deal with compared to the former alternative proposed here. Moreover, the representation of the entire system in the state-space for a control purposes will become more involved and not trivial.

Considering all these points, the virtual work of the system can be expressed as

$$\begin{aligned}\delta W^{\mathrm{nc}} = {} & f(t)\delta d(t) + \int_0^L Q(x,t)\delta w(x,t)\,\mathrm{d}x - \Big\{ B\int_0^L w_t(x,t)\delta w(x,t)\,\mathrm{d}x \\ & + C\int_0^L w_{xt}(x,t)\delta w(x,t)\,\mathrm{d}x + B\int_0^L v_t(x,t)\delta v(x,t)\,\mathrm{d}x + C\int_0^L v_{xt}(x,t)\delta v(x,t)\,\mathrm{d}x\Big\} \\ & + \Big\{\int_0^L \Delta(x-L+\varepsilon)F_{\text{tip-}z}(t)\delta w(x,t)\,\mathrm{d}x + \int_0^L \Delta(x-L+\varepsilon)F_{\text{tip-}y}(t)\delta v(x,t)\,\mathrm{d}x \\ & + \int_0^L \Delta(x-L+\varepsilon)F_{\text{tip-}x}(t)\delta u(x,t)\,\mathrm{d}x\Big\} + \Big\{\int_0^L \Delta(x-L+\varepsilon)F_{\text{tip-}x}(t)H\delta w_x(x,t)\,\mathrm{d}x \\ & + \int_0^L \Delta(x-L+\varepsilon)F_{\text{tip-}y}(t)H\delta\theta(x,t)\,\mathrm{d}x\Big\} - \Big\{C_z\int_0^L \Delta(x-L+\varepsilon)w_t(L,t)\delta w(x,t))\,\mathrm{d}x \\ & + C_x\int_0^L \Delta(x-L+\varepsilon)[u_t(L,t)+u_{t,\text{fric-}x}+w_{xt}(L,t)H]\delta u(x,t)\,\mathrm{d}x \\ & + C_y\int_0^L \Delta(x-L+\varepsilon)[v_t(L,t)+u_{t,\text{fric-}y}-\theta_t(L,t)H]\delta v(x,t)\,\mathrm{d}x\Big\} \\ & - \Big\{C_xH\int_0^L \Delta(x-L+\varepsilon)[u_t(L,t)+u_{t,\text{fric-}x}+w_{xt}(L,t)H]\delta w_x(x,t)\,\mathrm{d}x \\ & + C_yH\int_0^L \Delta(x-L+\varepsilon)[v_t(L,t)+u_{t,\text{fric-}y}-\theta_t(L,t)H]\delta\theta(x,t)\,\mathrm{d}x\Big\}, \end{aligned} \tag{5}$$

where $\delta(\cdot)$ denotes variation of the arguments. The above equation expresses the virtual work of the system due to; boundary control input force (first term), capacitive forces between tip-cantilever assembly and surface (second term), microcantilever damping terms in transversal and lateral directions (third term), piezoelectric forces of sample in all three directions (fourth term), moment and torsion due to piezoelectric force in the longitudinal and lateral directions (fifth term), material damping forces (sixth term), and moment and torsion due to material damping terms in the longitudinal and lateral directions (last term).

The extended Hamilton's principle can be expressed as

$$\int_{t_1}^{t_2} \delta(\mathrm{KE}-\mathrm{PE}+W^{\mathrm{nc}})\,\mathrm{d}t = 0. \tag{6}$$

Substituting Eqs. (3)–(5) into Eq. (6) yields the following partial differential equations for the motion of PFM:

(1) For vertical vibration of microcantilever:

$$\begin{aligned} & \rho[\ddot{d}(t)+w_{tt}(x,t)] + EI_{yy}w_{xxxx}(x,t) + Bw_t(x,t) + Cw_{xt}(x,t) \\ & \quad - C_xH\Delta_x(x-L+\varepsilon)[u_t(L,t)+w_{xt}(L,t)] + C_z\Delta(x-L+\varepsilon)w_t(L,t) \\ & \quad = Q(x,t) - \Delta_x(x-L+\varepsilon)HF_{\text{tip-}x}(t) + C_xH\Delta_x(x-L+\varepsilon)u_{t,\text{fric-}x} + \Delta(x-L+\varepsilon)F_{\text{tip-}z}(t). \end{aligned} \tag{7}$$

(2) For base motion:

$$m\ddot{d}(t) + \int_0^L \rho[\ddot{d}(t)+w_{tt}(x,t)]\,\mathrm{d}x + m_e[\ddot{d}(t)+w_{tt}(L,t)] = f(t). \tag{8}$$

(3) For lateral vibration of microcantilever:

$$\begin{aligned} & \rho v_{tt}(x,t) + EI_{zz}v_{xxxx}(x,t) + Bv_t(x,t) + Cv_{xt}(x,t) + C_y\Delta(x-L+\varepsilon)[v_t(L,t)-H\theta_t(L,t)] \\ & \quad = \Delta(x-L+\varepsilon)F_{\text{tip-}y}(t) - C_y\Delta(x-L+\varepsilon)u_{t,\text{fric-}y}. \end{aligned} \tag{9}$$

(4) For torsion of microcantilever:

$$J\theta_{tt}(x,t) - C_T\theta_{xx}(x,t) + C_yH\Delta(x-L+\varepsilon)[v_t(L,t) - H\theta_t(L,t)] = \Delta(x-L+\varepsilon)HF_{\text{tip-}y}(t) - C_yH\Delta(x-L+\varepsilon)u_{t,\text{fric-}y}. \tag{10}$$

(5) For longitudinal vibration of microcantilever:

$$\rho u_{tt}(x,t) - EAu_{xx}(x,t) + C_x\Delta(x-L+\varepsilon)[u_t(L,t) + Hw_{xt}(L,t)] = \Delta(x-L+\varepsilon)F_{\text{tip-}x}(t) - C_x\Delta(x-L+\varepsilon)u_{t,\text{fric-}x}, \tag{11}$$

along with the following boundary conditions

$$m_e[\ddot{d}(t) + w_{tt}(L,t)] - EI_{yy}w_{xxx}(L,t) + k_zw(L,t) = 0, \tag{12}$$

$$m_ev_{tt}(L,t) - EI_{zz}v_{xxx}(L,t) + k_y(v(L,t) - \theta(L,t)H) = -k_yu_{\text{fric-}y}, \tag{13}$$

$$m_eu_{tt}(L,t) + EAu_x(L,t) + k_x(u(L,t) + w_x(L,t)H) = -k_xu_{\text{fric-}x}, \tag{14}$$

$$EI_{yy}w_{xx}(L,t) - k_xH(u(L,t) + w_x(L,t)H) = k_xHu_{\text{fric-}x}, \tag{15}$$

$$C_T\theta_x(L,t) - k_yH(v(L,t) - H\theta(L,t)) = -k_yHu_{\text{fric-}y}, \tag{16}$$

and

$$w(0,t) = w_x(0,t) = v_{xx}(L,t) = v(0,t) = v_x(0,t) = u(0,t) = \theta(0,t) = 0. \tag{17}$$

The above equations indicate that the transversal bending is coupled to longitudinal displacement and lateral bending is coupled to torsional motion of microcantilever through geometrical terms, friction and piezoelectric forces acting at the end of beam (the terms in the right-hand side of Eqs. (7)–(11)). Moreover, the boundary conditions for those coupled motions are also coupled and nonhomogeneous.

4. Assumed mode model expansion

In order to numerically investigate the obtain equations of motion, we utilize assuming mode model (AMM) to discretize the original partial differential equations into the ordinary differential equations. Since boundary conditions in Eqs. (13)–(16) are nonhomogeneous, a new set of variables are defined in order to obtain homogenized boundary conditions. Then, assuming that variables are separable, a set of ordinary equations is obtained for different directions.

4.1. Coupled transversal–longitudinal displacement

As mentioned earlier, Eqs. (14) and (15) indicate that the coupled boundary conditions in longitudinal and transversal directions are nonhomogeneous. To remedy this complexity, the boundary conditions should be first homogenized. For this purpose, two new variables z and G are introduced with the following expressions:

$$w(x,t) = z(x,t) - u_{\text{fric-}x}F_1(x), \tag{18}$$

$$u(x,t) = G(x,t) - u_{\text{fric-}x}F_2(x), \tag{19}$$

where $F_i(x)$ $(i = 1,2)$ are geometrical functions. To determine these functions, Eqs. (18) and (19) are substituted into Eqs. (12), (14) and (15). Then, all boundary conditions are forced to be homogenized simultaneously in the new coordinates which result in the following conditions on geometrical functions F_1 and F_2:

$$F_1(0) = F_1'(0) = F_1(L) = F_1'(L) = F_1'''(L) = 0 \quad \text{and} \quad F_1''(L) = -\frac{k_xH}{EI_{yy}}, \tag{20}$$

$$F_2(0) = F_2'(0) = F_2(L) = 0 \quad \text{and} \quad F_2'(L) = \frac{k_x}{EA}. \tag{21}$$

These geometrical functions can be obtained as

$$F_1(x) = \frac{k_x H}{EI_{yy}L^3}\left(x^5 - \frac{7}{2}Lx^4 + 4L^2x^3 - \frac{3}{2}L^3x^2\right), \tag{22}$$

$$F_2(x) = \frac{k_x}{EAL}(x^2 - Lx). \tag{23}$$

Now, applying Eqs. (18) and (19) into the original equations of motion in the vertical and longitudinal directions (7), (8) and (11), the new equations can be written as

$$\begin{aligned}&\rho[\ddot{d}(t) + z_{tt}(x,t)] + EI_{yy}z_{xxxx}(x,t) + Bz_t(x,t) + Cz_{xt}(x,t)\\ &\quad - C_xH\Delta_x(x-L+\varepsilon)[G_t(L,t) + z_{xt}(L,t)] + C_z\Delta(x-L+\varepsilon)z_t(L,t) = \Pi_1(x,t),\end{aligned} \tag{24}$$

where

$$\begin{aligned}\Pi_1(x,t) = {} & Q(x,t) - \Delta_x(x-L+\varepsilon)HF_{\text{tip-}x}(t) + C_xH\Delta_x(x-L+\varepsilon)u_{t,\text{fric-}x}\\ &+ \Delta(x-L+\varepsilon)F_{\text{tip-}z}(t) + \rho u_{tt,\text{fric-}x}F_1(x) + EI_{yy}u_{\text{fric-}x}F_1''''(x) + Bu_{t,\text{fric-}x}F_1(x)\\ &+ Cu_{t,\text{fric-}x}F_1'(x) - C_xH\Delta_x(x-L+\varepsilon)u_{t,\text{fric-}x}[F_2(L) + F_1'(L)] + C_z\Delta(x-L+\varepsilon)u_{t,\text{fric-}x}F_1(L),\end{aligned} \tag{25}$$

$$m\ddot{d}(t) + \int_0^L \rho[\ddot{d}(t) + z_{tt}(x,t)]\,\mathrm{d}x + m_e[\ddot{d}(t) + z_{tt}(L,t)] = \Pi_2(x,t), \tag{26}$$

where

$$\Pi_2(x,t) = f(t) + \int_0^L \rho u_{tt,\text{fric-}x}F_1(x)\,\mathrm{d}x + m_e u_{tt,\text{fric-}x}F_1(L), \tag{27}$$

and finally,

$$\rho G_{tt}(x,t) - EAG_{xx}(x,t) + C_x\Delta(x-L+\varepsilon)[G_t(L,t) + Hz_{xt}(L,t)] = \Pi_3(x,t), \tag{28}$$

where

$$\begin{aligned}\Pi_3(x,t) = {} & \Delta(x-L+\varepsilon)F_{\text{tip-}x}(t) - C_x\Delta(x-L+\varepsilon)u_{t,\text{fric-}x} + \rho u_{tt,\text{fric-}x}F_2(x)\\ &- EAu_{\text{fric-}x}F_2''(x) + C_x\Delta(x-L+\varepsilon)u_{t,\text{fric-}x}[F_2(L) + HF_1'(L)],\end{aligned} \tag{29}$$

with the following boundary conditions:

$$m_e[\ddot{d}(t) + z_{tt}(L,t)] - EI_{yy}z_{xxx}(L,t) + k_z z(L,t) = 0, \tag{30}$$

$$m_e G_{tt}(L,t) + EAG_x(L,t) + k_x(G(L,t) + z_x(L,t)H) = 0, \tag{31}$$

$$EI_{yy}z_{xx}(L,t) - k_xH(G(L,t) + z_x(L,t)H) = 0, \tag{32}$$

$$z(0,t) = z_x(0,t) = G(0,t) = 0. \tag{33}$$

Now, utilizing above equations, the natural frequencies, mode shapes and time response of microcantilever for coupled motion can be obtained.

4.1.1. Frequency equation, orthogonality conditions and mode shapes

In order to obtain natural frequencies and mode shapes of the system, the eigenvalue problem associated with the transversal–longitudinal vibration of beam is obtained through applying free and undamped conditions in Eqs. (24) and (29), which results in

$$\rho z_{tt}(x,t) + EI_{yy}z_{xxxx}(x,t) = 0 \tag{34}$$

and

$$\rho G_{tt}(x,t) - EAG_{xx}(x,t) = 0. \tag{35}$$

The separation of variables can be assumed in the form of

$$z(x,t) = \Phi(x)e^{i\omega t} \quad \text{and} \quad G(x,t) = \Lambda(x)e^{i\omega t}, \tag{36}$$

where $\Phi(x)$ and $\Lambda(x)$ are the mode shapes of the microcantilever beam with a tip mass and ω is the natural frequency of the system. Applying Eq. (36) into Eqs. (34) and (35) results in the following differential equations:

$$\Phi''''(x) - \lambda^4\Phi(x) = 0, \tag{37}$$

$$\Lambda''(x) + \xi^2\Lambda(x) = 0, \tag{38}$$

where

$$\lambda^4 = \frac{\rho\omega^2}{EI_{yy}} \quad \text{and} \quad \xi = \sqrt{I_{yy}/A}\lambda^2. \tag{39}$$

The solutions for Eqs. (37) and (38) can be written, respectively, as

$$\Phi(x) = K_1[\sin(\lambda x) - \sinh(\lambda x)] + K_2[\cos(\lambda x) - \cosh(\lambda x)], \tag{40}$$

$$\Lambda(x) = K_3 \sin(\lambda^2\sqrt{I_{yy}/A})x, \tag{41}$$

where K_1, K_2 and K_3 are coefficients of mode shapes to be determined.

Inserting Eqs. (40) and (41) into boundary conditions (30)–(32), the results can be written in the matrix form as

$$\begin{bmatrix} A_{11} & A_{12} & A_{13} \\ A_{21} & A_{22} & A_{23} \\ A_{31} & A_{32} & A_{33} \end{bmatrix} \begin{bmatrix} K_1 \\ K_2 \\ K_3 \end{bmatrix} = 0, \tag{42}$$

where

$$A_{11} = -EI_{yy}\lambda^3\Phi_1'''(L) - (m_e\omega^2 - k_z)\Phi_1(L),$$

$$A_{12} = -EI_{yy}\lambda^3\Phi_2'''(L) - (m_e\omega^2 - k_z)\Phi_2(L),$$

$$A_{13} = 0,$$

$$A_{21} = -\frac{EI_{yy}}{H}\lambda^2\Phi_1'''(L),$$

$$A_{22} = -\frac{EI_{yy}}{H}\lambda^2\Phi_2''(L),$$

$$A_{23} = -m_e\omega^2 \sin \xi L + EA\xi \cos \xi L,$$

$$A_{31} = \frac{EI_{yy}}{H}\lambda^2\Phi_1''(L) + k_xH\lambda\Phi'(L),$$

$$A_{32} = \frac{EI_{yy}}{H}\lambda^2\Phi_2''(L) + k_xH\lambda\Phi_2'(L),$$

$$A_{33} = k_x \sin \xi L, \tag{43}$$

and

$$\Phi_1(L) = \Phi_2'''(L) = \sin\ \lambda L - \sinh\ \lambda L,$$

$$\Phi_1'(L) = \Phi_2(L) = \cos\ \lambda L - \cosh\ \lambda L,$$

$$\Phi_1''(L) = \Phi_2'(L) = -\sin\ \lambda L - \sinh\ \lambda L,$$

$$\Phi_1'''(L) = \Phi_2''(L) = -\cos\ \lambda L - \cosh\ \lambda L. \tag{44}$$

The frequency equation can now be obtained by equating the determinant of Eq. (42) to zero, which yields:

$$\begin{aligned}
&- EI_{yy}\lambda^3\Phi_1'''(L)\left\{-\frac{EI_{yy}}{H}k_x\lambda^2\Phi_2''(L)\sin(\xi L) + m_e\omega^2\frac{EI_{yy}}{H}\lambda^2\sin(\xi L)\Phi_2''(L)\right.\\
&\left.+ m_e\omega^2\lambda k_x H\sin(\xi L)\Phi_2'(L) - E^2\frac{AI_{yy}}{H}\xi\cos(\xi L)\lambda^2\Phi_2''(L) - EAk_xH\lambda\xi\cos(\xi L)\Phi_2'(L)\right\}\\
&+ (m_e\omega^2 - k_z)\left\{\frac{EI_{yy}}{H}\lambda^2\sin(\xi L)\Phi_2''(L)\Phi_1(L)(k_x - m_e\omega^2) - m_e\omega^2\lambda k_x H\sin(\xi L)\Phi_2'(L)\Phi_1(L)\right.\\
&\left.+ E^2\frac{AI_{yy}}{H}\xi\cos(\xi L)\lambda^2\Phi_2''(L)\Phi_1(L) + EAk_xH\lambda\xi\cos(\xi L)\Phi_2'(L)\Phi_1(L)\right\}\\
&+ EI_{yy}\lambda^3\Phi_2'''(L)\left\{-\frac{EI_{yy}}{H}\lambda^2\Phi_2''(L)k_x\sin(\xi L) + m_e\omega^2\frac{EI_{yy}}{H}\lambda^2\sin(\xi L)\Phi_1''(L)\right.\\
&\left.+ m_e\omega^2\lambda k_x H\sin(\xi L)\Phi_1'(L) - E^2\frac{AI_{yy}}{H}\xi\cos(\xi L)\lambda^2\Phi_1''(L) - EAk_xH\lambda\xi\cos(\xi L)\Phi_1'(L)\right\}\\
&- (m_e\omega^2 - k_z)\left\{\frac{EI_{yy}}{H}\lambda^2\sin(\xi L)\Phi_1''(L)\Phi_2(L)(k_x - m_e\omega^2) - m_e\omega^2\lambda k_x H\sin(\xi L)\Phi_1'(L)\Phi_2(L)\right.\\
&\left.+E^2\frac{AI_{yy}}{H}\xi\cos(\xi L)\lambda^2\Phi_1''(L)\Phi_2(L) + EAk_xH\lambda\xi\cos(\xi L)\Phi_1'(L)\Phi_2(L)\right\} = 0.
\end{aligned} \tag{45}$$

In order to determine the coefficients of mode shapes, K_1 and K_3 can be derived from Eq. (42) in terms of K_2 as

$$K_1 = -\frac{A_{12}}{A_{11}}K_2, \tag{46}$$

$$K_3 = \frac{1}{A_{23}}\left(A_{21}\frac{A_{12}}{A_{11}} - A_{22}\right)K_2. \tag{47}$$

To obtain unique solution for these coefficients, orthonormality between mode shapes can be utilized. For the boundary conditions considered here, this condition is stated as

$$\int_0^L m(x)[\Phi_i(x)\Phi_j(x) + \Lambda_i(x)\Lambda_j(x)]\,\mathrm{d}x + m_e\Phi_i(L)\Phi_j(L) + m_e\Lambda_i(L)\Lambda_j(L) = \delta_{ij}, \tag{48}$$

where δ_{ij} is the Kronecker delta.

4.1.2. Forced motion analysis of coupled transversal/longitudinal motion

Using expansion theorem for the beam vibration analysis, the expressions for the transverse and longitudinal displacements become:

$$z(x,t) = \sum_{i=1}^{\infty}\Phi_i(x)q_i(t), \tag{49}$$

$$G(x,t) = \sum_{i=1}^{\infty}\Lambda_i(x)q_i(t), \tag{50}$$

where $q_i(t)$ are the generalized time-dependent coordinates. Now, inserting Eqs. (49) and (50) into Eqs. (24)–(29) and after some manipulations, the discretized model for the transversal vibration and base motion of microcantilever can be written, respectively, as

$$A_i\ddot{d}(t)+\sum_{j=1}^{\infty}B_{ij}\ddot{q}_j(t)+\sum_{j=1}^{\infty}C_{ij}\dot{q}_j(t)+\sum_{j=1}^{\infty}D_{ij}q_j(t)=f_i(t),\quad i=1,2,\ldots,\infty, \tag{51}$$

where

$$A_i=\int_0^L\rho\Phi_i(x)\,\mathrm{d}x,\quad B_{ij}=\int_0^L\rho\Phi_i(x)\Phi_j(x)\,\mathrm{d}x,$$

$$C_{ij}=\int_0^L\Phi_i(x)[B\Phi_j(x)+C\Phi_j'(x)]\,\mathrm{d}x+C_xH\Phi_i'(L-\varepsilon)[\Phi_j'(L)+\Lambda_j(L)]+C_z\Phi_i(L-\varepsilon)\Phi_j(L),$$

$$D_{ij}=EI_{yy}\int_0^L\Phi_i(x)\Phi_j''''(x)\,\mathrm{d}x,$$

$$f_i(t)=\int_0^L\Phi_i(x)\Pi_1(x,t)\,\mathrm{d}x, \tag{52}$$

and base motion can be expressed as

$$\Psi\ddot{d}(t)+\sum_{i=1}^{\infty}L_i\ddot{q}_i(t)=\Pi_2(x,t), \tag{53}$$

where

$$\Psi=(m+m_e+\rho L),\quad L_i=\int_0^L\rho\Phi_i(x)\,\mathrm{d}x+m_e\Phi_i(L). \tag{54}$$

The truncated n-mode description for Eqs. (51) and (53) can now be presented in the following matrix form:

$$\mathbf{M}\ddot{\mathbf{q}}+\mathbf{C}\dot{\mathbf{q}}+\mathbf{K}\mathbf{q}=\mathbf{F}\mathbf{u}, \tag{55}$$

where

$$\mathbf{M}=\begin{bmatrix}\Psi & L_1 & L_2 & \cdots & L_n\\ A_1 & B_{11} & B_{12} & \cdots & B_{1n}\\ A_2 & B_{21} & B_{22} & \cdots & B_{2n}\\ \vdots & \vdots & \vdots & \ddots & \vdots\\ A_n & B_{n1} & B_{n2} & \cdots & B_{nn}\end{bmatrix}\quad \mathbf{C}=\begin{bmatrix}0 & 0 & 0 & \cdots & 0\\ 0 & C_{11} & C_{12} & \cdots & C_{1n}\\ 0 & C_{21} & C_{22} & \cdots & C_{2n}\\ \vdots & \vdots & \vdots & \ddots & \vdots\\ 0 & C_{n1} & C_{n2} & \cdots & C_{nn}\end{bmatrix},$$

$$\mathbf{K}=\begin{bmatrix}0 & 0 & 0 & \cdots & 0\\ 0 & D_{11} & D_{12} & \cdots & D_{1n}\\ 0 & D_{21} & D_{22} & \cdots & D_{2n}\\ \vdots & \vdots & \vdots & \ddots & \vdots\\ 0 & D_{n1} & D_{n2} & \cdots & D_{nn}\end{bmatrix}\quad \mathbf{q}=\begin{Bmatrix}d(t)\\ q_1(t)\\ q_2(t)\\ \vdots\\ q_n(t)\end{Bmatrix},$$

$$\mathbf{F}=\begin{bmatrix}1 & 0 & 0 & F_4\\ 0 & \overline{F}_{11} & \overline{F}_{21} & \overline{F}_{31}\\ 0 & \overline{F}_{12} & \overline{F}_{22} & \overline{F}_{32}\\ \vdots & \vdots & \vdots & \vdots\\ 0 & \overline{F}_{1n} & \overline{F}_{2n} & \overline{F}_{3n}\end{bmatrix}\quad \mathbf{u}=\begin{Bmatrix} f(t)\\ V(t)\\ \dot{V}(t)\\ \ddot{V}(t)\end{Bmatrix}, \tag{56}$$

where

$$\begin{aligned}
F_4 &= \frac{\mu_x}{k_x}\beta a\left[\int_0^L \rho F_1(x)\,\mathrm{d}x + m_e F_1(L)\right]\\
\bar{F}_{1i} &= \beta a\left[\frac{\mu_x}{k_x} EI_{yy}\int_0^L \Phi_i(x)F_1''''(x)dx + H\Phi_i'(L-\varepsilon) + \Phi_i(L-\varepsilon)\right]\\
\bar{F}_{2i} &= \beta a\frac{\mu_x}{k_x}[B\int_0^L \Phi_i(x)F_1(x)\,\mathrm{d}x + C\int_0^L \Phi_i(x)F_1'(x)\,\mathrm{d}x\\
&\quad + C_x H\Phi_i'(L-\varepsilon)(F_2(L)+F_1'(L)-1) + C_z\Phi_i(L-\varepsilon)F_1(L)]\\
\bar{F}_{3i} &= \beta a\frac{\mu_x}{k_x}\int_0^L \rho\Phi_j(x)F_1(x)\,\mathrm{d}x \quad i=1,2,\ldots,\infty
\end{aligned} \tag{57}$$

Eq. (55) can now be written in the form of state-space as

$$\dot{\mathbf{X}} = \Xi\mathbf{X} + \Gamma\mathbf{u}, \tag{58}$$

where

$$\Xi=\begin{bmatrix}0 & I\\ -M^{-1}K & -M^{-1}C\end{bmatrix}_{2(k+1)\times 2(k+1)},\quad \Gamma=\begin{bmatrix}0\\ M^{-1}F\end{bmatrix}_{2(k+1)\times 1},\quad C=\begin{bmatrix}0\\ M^{-1}\end{bmatrix}_{2(k+1)\times 1}\ \text{and}\ X=\begin{Bmatrix}q\\ \dot{q}\end{Bmatrix}_{2(k+1)\times 1}. \tag{59}$$

The longitudinal vibration of system can also be expressed as

$$\sum_{j=1}^{\infty} P_{ij}\ddot{q}_j(t) + \sum_{j=1}^{\infty} R_{ij}\dot{q}_j(t) + \sum_{j=1}^{\infty} U_{ij}q_j(t) = Y_i(t),\quad i=1,2,\ldots,\infty, \tag{60}$$

where

$$P_{ij}=\int_0^L \rho\Lambda_i(x)\Lambda_j(x)\,\mathrm{d}x,\quad R_{ij}=C_x\Lambda_i(L-\varepsilon)[\Lambda_j(L)+H\Phi_j'(L)],$$

$$U_{ij}=-EA\int_0^L \Lambda_i(x)\Lambda_j''(x)\,\mathrm{d}x,\quad Y_i(t)=\int_0^L \Lambda_i(x)\Pi_3(x,t)\,\mathrm{d}x, \tag{61}$$

and the truncated n-mode description for Eqs. (60) is as follows:

$$\mathbf{M_L}\ddot{\mathbf{q}}_\mathbf{L} + \mathbf{C_L}\dot{\mathbf{q}}_\mathbf{L} + \mathbf{K_L}\mathbf{q_L} = \mathbf{F_L}\mathbf{u_L}, \tag{62}$$

where

$$\mathbf{M_L}=\begin{bmatrix}P_{11} & P_{12} & \ldots & P_{1n}\\ P_{21} & P_{22} & \ldots & P_{2n}\\ \vdots & \vdots & \ddots & \vdots\\ P_{n1} & P_{n2} & \ldots & P_{nn}\end{bmatrix}\quad \mathbf{C_L}=\begin{bmatrix}R_{11} & R_{12} & \ldots & R_{1n}\\ R_{21} & R_{22} & \ldots & R_{2n}\\ \vdots & \vdots & \ddots & \vdots\\ R_{n1} & R_{n2} & \ldots & R_{nn}\end{bmatrix},$$

$$\mathbf{K_L} = \begin{bmatrix} U_{11} & U_{12} & \dots & U_{1n} \\ U_{21} & U_{22} & \dots & U_{2n} \\ \vdots & \vdots & \ddots & \vdots \\ U_{n1} & U_{n2} & \dots & U_{nn} \end{bmatrix} \quad \mathbf{q_L} = \begin{Bmatrix} q_1(t) \\ q_2(t) \\ \vdots \\ q_n(t) \end{Bmatrix},$$

$$\mathbf{F_L} = \begin{bmatrix} F_{L-11} & F_{L-21} & F_{L-31} \\ \vdots & \vdots & \vdots \\ F_{L-1n} & F_{L-2n} & F_{L-3n} \end{bmatrix} \quad \mathbf{u_L} = \begin{Bmatrix} V(t) \\ \dot{V}(t) \\ \ddot{V}(t) \end{Bmatrix}, \tag{63}$$

where

$$F_{L-1i} = \beta a \left[\Phi_i(L-\varepsilon) - \frac{\mu_x}{k_x} EA \int_0^L \Phi_i(x) F_2''(x)\,\mathrm{d}x \right],$$

$$F_{L-2i} = \beta a \frac{\mu_x}{k_x} C_x \Phi_i(L-\varepsilon)[F_2(L) + HF_1'(L) - 1],$$

$$F_{L-3i} = \beta a \frac{\mu_x}{k_x} \int_0^L \rho \Phi_i(x) F_2(x)\,\mathrm{d}x. \tag{64}$$

Finally, Eq. (55) can be expressed in the form of state-space as

$$\dot{\mathbf{X}}_\mathbf{L} = \Xi_L \mathbf{X_L} + \Gamma_L \mathbf{u_L}, \tag{65}$$

where

$$\Xi_L = \begin{bmatrix} 0 & I \\ -M_L^{-1}K_L & -M_L^{-1}C_L \end{bmatrix}_{2(k+1)\times 2(k+1)}, \quad \Gamma_L = \begin{bmatrix} 0 \\ M_L^{-1}F_L \end{bmatrix}_{2(k+1)\times 1}, \quad C_L = \begin{bmatrix} 0 \\ M_L^{-1} \end{bmatrix}_{2(k+1)\times 1}$$

and

$$X_L = \begin{Bmatrix} q_L \\ \dot{q}_L \end{Bmatrix}_{2(k+1)\times 1}. \tag{66}$$

4.2. Coupled lateral bending–torsion vibrations

Similar to pervious problem, torsion and lateral bending vibrations are also coupled through geometrical terms, friction and piezoelectric forces. The coupling terms appear in the right-hand side of Eqs. (9) and (10) as well as coupled terms in the boundary conditions (13) and (16). Comparing the eigenvalue problems for lateral bending–torsion and transversal bending–longitudinal motions (Eqs. (67)–(70)) reveals that the nature of equations for lateral and transversal bending and that of longitudinal and torsion are similar. The differences are related to constant coefficients of corresponding partial differential equations. Applying the similar procedure explained in the preceding section, the mode shapes, frequency equation, orthogonality condition and state-space representation for the coupled lateral bending–torsion motion can be also obtained. For the sake of briefness and undue complication, we do not provide the details here.

$$\rho v_{tt}(x,t) + EI_{zz} v_{xxxx}(x,t) + Bv_t(x,t) + Cv_{xt}(x,t) = 0, \tag{67}$$

$$\rho[\ddot{d}(t) + w_{tt}(x,t)] + EI_{yy} w_{xxxx}(x,t) - Q(x,t) + Bw_t(x,t) + Cw_{xt}(x,t) = 0, \tag{68}$$

$$J\theta_{tt}(x,t) - C_T \theta_{xx}(x,t) = 0, \tag{69}$$

$$\rho u_{tt}(x,t) - EAu_{xx}(x,t) = 0. \tag{70}$$

Table 1
Physical parameters of the system.

Properties	Symbol	Value	Unit
Beam length	L	460	μm
Beam thickness	t	2	μm
Beam width	b	50	μm
Beam density	ρ	2330	kg/m
Beam elastic modulus	E	120	GPa
Beam moment of inertia	I	3.33×10^{-23}	m^4
Tip height	H	20×10^{-6}	M
Tip mass	m_e	3×10^{-10}	kg
Base mass	m	0.001	kg
Beam viscous damping	B	1×10^{-8}	kg/s
Beam structural damping	C	1×10^{-8}	kg/ms
Contact radius	a	50×10^{-6}	m
Piezoelectric coefficient of material	β	40	N/mV

Table 2
Natural frequencies of microcantilever for vertical piezoresponse force microscopy.

	$k_z=0$	$k_z=1$	$k_z=3$	$k_z=5$	$k_z=10$	$k_z=100$	$k_z=1000$	$k_z=2000$
$\omega_1(10^6)$	0.0687	0.1838	0.2459	0.2665	0.2838	0.3001	0.3017	0.3018
$\omega_2(10^6)$	0.4310	0.4777	0.5720	0.6483	0.7887	0.9575	0.9763	0.9773
$\omega_3(10^6)$	1.2069	1.2227	1.2574	1.2951	1.3958	1.9425	2.0323	2.0368

Table 3
Natural frequencies of microcantilever for longitudinal piezoresponse force microscopy.

	$k_x=0$	$k_x=1$	$k_x=3$	$k_x=5$	$k_x=10$	$k_x=100$	$k_x=1000$	$k_x=2000$
$\omega_1(10^6)$	0.0687	0.0697	0.0714	0.0730	0.0765	0.5183	0.5790	0.5848
$\omega_2(10^6)$	0.4310	0.4329	0.4364	0.4399	0.4478	1.3150	1.4311	1.4446
$\omega_3(10^6)$	1.2069	1.2087	1.2122	1.2156	1.2238	2.4878	2.6629	2.6867

Table 4
Natural frequencies of microcantilever for vertical-longitudinal piezoresponse force microscopy where $k=k_x=k_z$.

	$k=0$	$k=1$	$k=3$	$k=5$	$k=10$	$k=100$	$k=1000$	$k=2000$
$\omega_1(10^6)$	0.0687	0.1838	0.2466	0.2685	0.2898	0.3539	0.4200	0.4218
$\omega_2(10^6)$	0.4310	0.4791	0.5741	0.6497	0.7686	1.0107	1.1569	1.1791
$\omega_3(10^6)$	1.2069	1.2227	1.2574	1.2951	1.3958	1.9425	2.0323	2.0368

5. Numerical results and discussions

Based on the modeling procedure described above, a numerical simulation procedure is adopted to study the variation of natural frequency, mode shape and time response of system with respect to viscoelastic and piezoelectric properties of materials. Table 1 lists the parameter values used for the numerical simulations.

For the simulation purpose, the equation of motions is truncated into only three modes. The eigenvalue problem associated with the transversal–longitudinal motion of beam is utilized to determine natural frequencies of microcantilever. Tables 2–4 list the natural frequency of the beam for; with only vertical spring (vertical PFM), with only longitudinal spring (longitudinal PFM), and with combined vertical–longitudinal

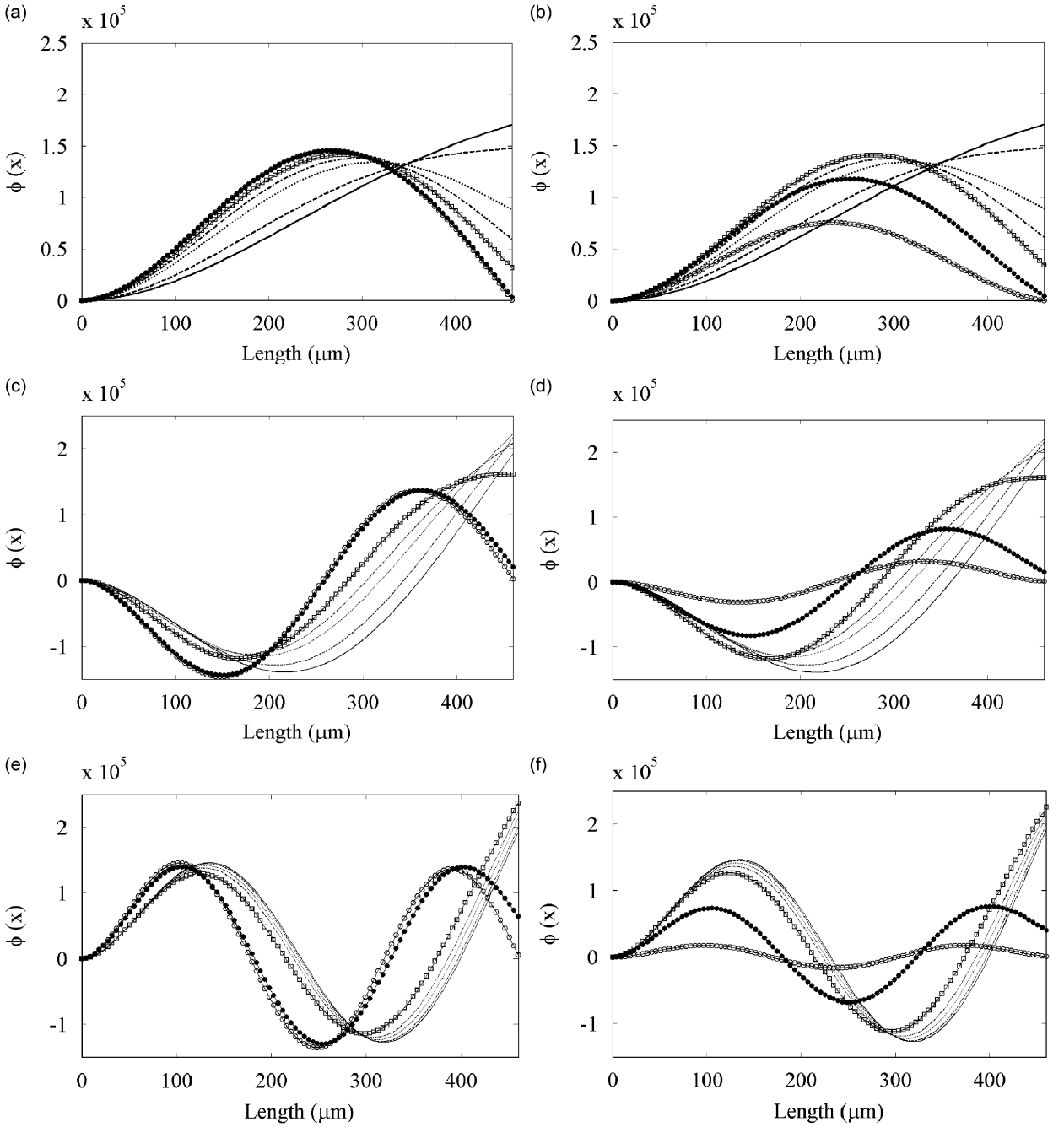

Fig. 4. Bending mode shapes of microcantilever for: (a) first mode of vertical, (b) first mode of vertical–longitudinal, (c) second mode of vertical, (d) second mode of vertical–longitudinal, (e) third mode of vertical, and (f) third mode of vertical–longitudinal piezoresponse force microscopy; where —: $k = 0$; – – –: $k = 1$; - - - - - -: $k = 3$; – - – -: $k = 5$; —□—: $k = 10$; —●—: $k = 100$; —○—: $k = 1000$; for $k = k_z$ (a, c and e) and for $k = k_x = k_z$ (b, d and f). The units of k_x and k_z are (N/m).

springs (vertical–longitudinal PFM), respectively. Results indicate that in vertical PFM, with the increase in sample spring constant, the natural frequency of microcantilever increases for all three mode shapes (see Table 2). Similar trend is seen for the natural frequency of longitudinal PFM (see Table 3). Results demonstrate that the variation of natural frequency with respect to the stiffness of spring show more smooth trend in vertical PFM compared to longitudinal one. In vertical–longitudinal PFM, the increase in the natural frequency is very small for the smaller spring constants; however, for the spring constant higher than 100 N/m the natural frequency for all three modes shows significant increase. At this range, longitudinal system displays higher natural frequency when compared to vertical PFM. Table 4 lists the natural frequency of the microcantilever for vertical–longitudinal PFM.

Fig. 4a depicts the first transversal mode shape of microcantilever in vertical system for different equivalent sample spring constants. It is seen that the mode shape of microcantilever is heavily dependent upon the elastic properties of sample. Due to presence of tip mass, mode shape show concave curvature for $k_z = 0$ at the end of beam. As the spring constant increases in the vertical direction, the radius of curvature decreases accordingly. This implies that higher spring constant makes more restriction at the end of microcantilever. Therefore, the clamped-free condition of the beam is converted into clamped-pinned condition for stiffer samples. Fig. 4b presents the mode shape of microcantilever beam in vertical–longitudinal PFM. The presence of longitudinal spring at stiffer material (higher spring constants) significantly affects the shape of curvature at the entire

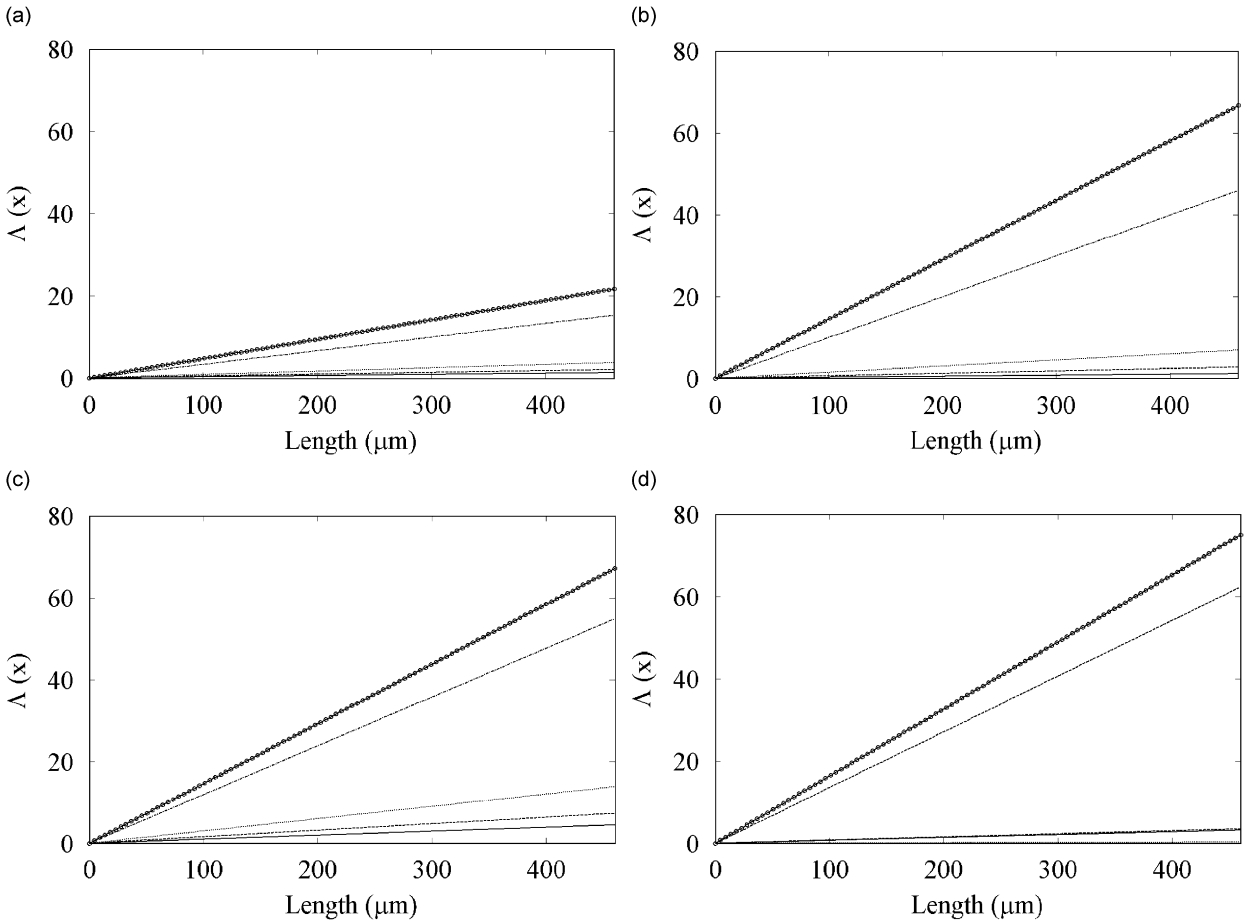

Fig. 5. Longitudinal mode shapes of microcantilever for: (a) first mode of longitudinal, (b) first mode of vertical–longitudinal, (c) third mode of longitudinal, and (d) third mode of vertical–longitudinal piezoresponse force microscopy; where —: $k = 3$; – – –: $k = 5$; ------: $k = 10$; - - - -: $k = 100$; —o—: $k = 1000$; for $k = k_z$ (a and c) and for $k = k_x = k_z$ (b and d). The units of k_x and k_z are (N/m).

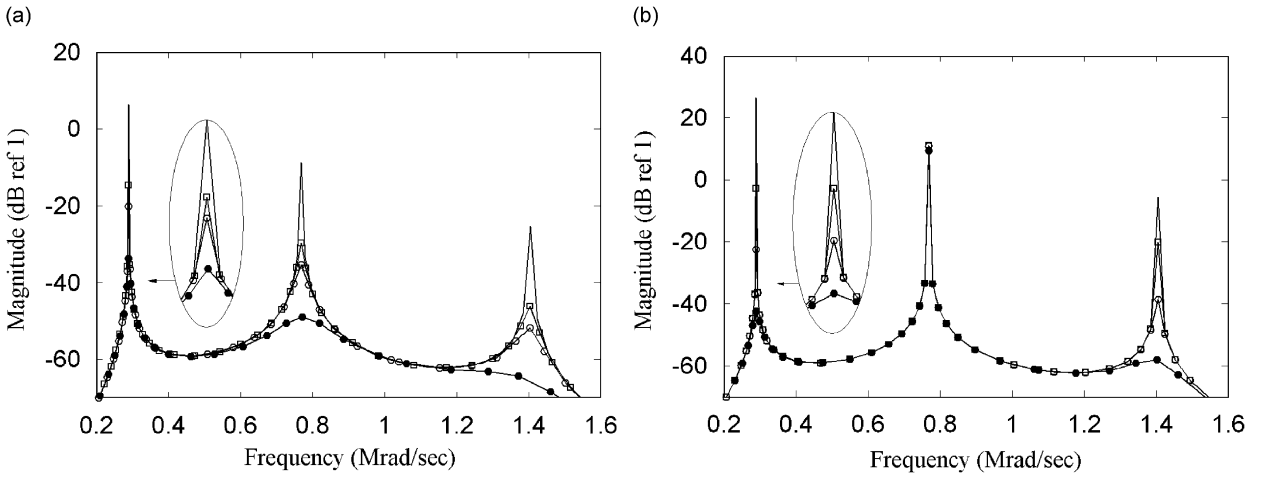

Fig. 6. Modal frequency response plot of microcantilever tip displacements at $k_x = k_z = 10\,\mathrm{N/m}$ and for four different damping ratios in: (a) transversal direction without longitudinal term (—: $C_z = 10^{-7}$; —□—: $C_z = 5\times10^{-7}$; —○—: $C_z = 10^{-6}$; and —●—: $C_z = 5\times10^{-6}$) and (b) longitudinal direction without transversal term (—: $C_x = 0$; —□—: $C_x = 10^{-11}$; —○—: $C_x = 10^{-10}$; and —●—: $C_x = 5\times10^{-9}$). The units of damping coefficients are (N s/m).

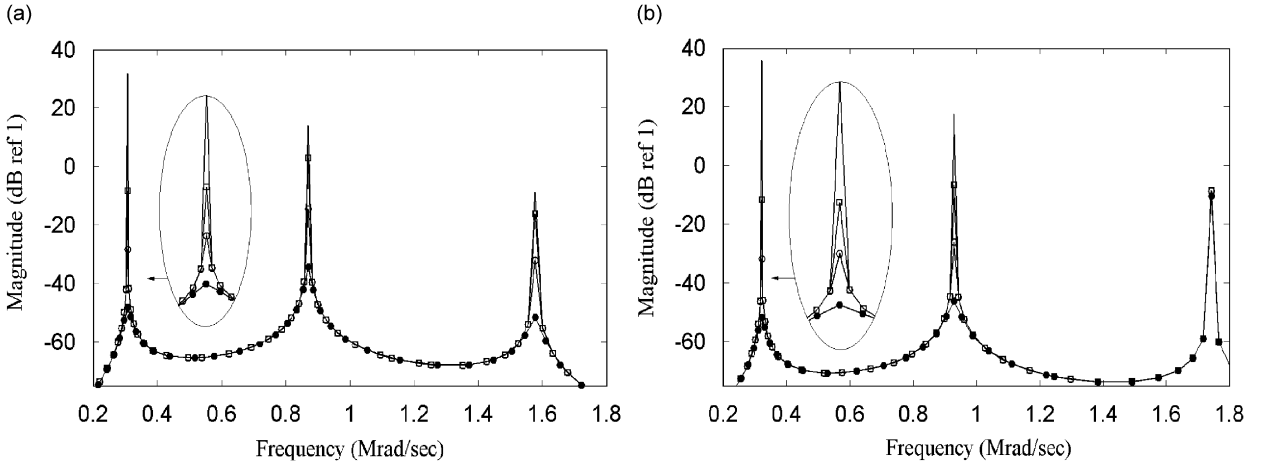

Fig. 7. Modal frequency response plot of microcantilever tip displacements for four damping ratios in longitudinal direction (without transversal term) and two spring constants: (a) $k_x = k_z = 20\,\mathrm{N/m}$ and (b) $k_x = k_z = 35\,\mathrm{N/m}$; where (—: $C_x = 0$; —□—: $C_x = 10^{-11}$; —○—: $C_x = 10^{-10}$; and —●—: $C_x = 5\times10^{-9}$). The units of damping coefficients are (N s/m).

length of beam compared to vertical spring. At this condition, the amplitude of vibration decreases significantly.

Figs. 4c–d depict the mode shapes of microcantilever for second natural frequency in vertical and vertical–longitudinal PFM, respectively. Results demonstrate that the amplitude of mode shape at the end of microcantilever increases for smaller values of spring constants. However, for higher spring constants, as expected, the amplitude of vibration decreases significantly. The reason is that as the constraint force is applied at the free end of the beam, the first extremum point of mode shapes moves left side with the increase in the spring constants. This results in the upward shift in the mode shapes of the beam with change in the slope of curvature at the end of microcantilever. As the spring force increases, the slope decreases accordingly. Finally, at some points spring force can overcome this shift which leads to decrease in the amplitude of vibration. Similar trend can be observed for the third mode shape of microcantilever (see Fig. 4e–f).

Figs. 5a–b depict the first longitudinal mode shape of microcantilever for longitudinal and vertical–longitudinal PFM, respectively. Results indicate that at higher spring constants the effect of coupling could have a

significant impact on the longitudinal mode shape of microcantilever. However, with the increase in the natural frequency of the system, the importance of coupling effect on the longitudinal vibration of microcantilever decreases accordingly (see Fig. 5c–d for the mode shape of microcantilever at third natural frequency of system).

Fig. 6a shows modal frequency response plot of microcantilever tip displacements at $k_x = k_z = 10\,\mathrm{N/m}$ at four different damping ratios in the transversal direction where the damping term in the longitudinal direction is not taken into account. As expected, with the increase of damping coefficient, the amplitude of vibration decreases such that for $C_z = 5 \times 10^{-6}\,\mathrm{N\,S/m}$ the effect of third resonant frequency is vanished. Along this line, the effect of longitudinal damping term on the vibration of microcantilever is shown in Fig. 6b. It is seen that the modal frequency of microcantilever in the presence of longitudinal damping term shows similar trend as observed in the previous case. More especially, Fig. 6b demonstrates that at $k_x = k_z = 10\,\mathrm{N/m}$, the resonance frequency of discrete system (tip-sample junction) reaches the second resonance frequency of the microcantilever. For this reason, the damping term does not influence the vibration amplitude at this frequency. Finally, Fig. 7 illustrates the effect of longitudinal damping term on the modal frequency of microcantilever at two different spring constants. The amplitude of vibration at $k_x = k_z = 20\,\mathrm{N/m}$ decreases for all three resonance frequencies; however, at $k_x = k_z = 35\,\mathrm{N/m}$ the resonance frequency of sample reaches the third resonance frequency of microcantilever.

In summary, it is shown that in vector PFM, the effect of coupling terms such as spring and damping terms significantly affect the natural frequencies and mode shapes of microcantilever. It is also observed that depending on the viscoelastic properties of sample; the resonance frequency of sample can reach one of resonance frequency of microcantilever. This results in un-damped vibrating condition in the corresponding frequency.

6. Conclusions

For materials with arbitrary crystallographic orientations, the vibration of microcantilever used in the PFM may experience combined motions in the vertical–longitudinal and/or lateral-torsional directions. In this study, a comprehensive dynamic model was proposed for a vector PFM with combined motions. It was shown that PFM can be represented as a set of partial differential equations which can be transferred into ordinary differential equations using assumed mode method. The PFM system was also written in the state-state representation form. It was shown that neglecting the coupling terms can affect the dynamic response of the system significantly. Moreover, effects of spring constant and damping coefficient of material in the vibration of microcantilever were studied in more detail. Results demonstrated that materials with different mechanical properties can induce different constraints at the free end of microcantilever, and materials with higher stiffness can change the clamped-free condition of cantilever into clamped-pinned condition.

Acknowledgments

The materials presented here are based upon work supported by the National Science Foundation CAREER Grant no. CMMI-0238987.

Disclaimer: Any opinions, findings, and conclusions or recommendations expressed in this material are those of the authors and do not necessarily reflect the views of the National Science Foundation.

References

[1] T. Tybell, P. Paruch, T. Giamarchi, J.-M. Triscone, Domain wall creep in epitax ferroelectric $Pb(Zr_{0.2}Ti_{0.8})O_3$ thin film, *Physical Review Letters* 89 (2002) 097601 (1–4).

[2] K. Terabe, M. Nakamura, S. Takekawa, K. Kitamura, S. Higuchi, Y. Gotoh, Y. Cho, Microscale to nanoscale ferroelectric domain and surface engineering of a near stoichiometric $LiNbO_3$ crystal, *Applied Physics Letters* 82 (3) (2003) 433–435.

[3] S. Kalinin, D. Bonnell, T. Alvarez, X. Lei, Z. Hu, J. Ferris, Atomic polarization and local reactivity on ferroelectric surfaces: a new route toward complex nanostructures, *Nano Letters* 2 (2004) 589–593.

[4] S. Kalinin, E. Karapetian, M. Kachanov, Nanoelectromechanics of piezoresponse force microscopy, *Physical Review B* 70 (2004) 184101 (1–24).

[5] E. Dupas, G. Gremaud, A.J. Kulik, J.L. Loubet, High-frequency mechanical spectroscopy with an atomic force microscope, *Review of Scientific Instruments* 72 (2001) 3891–3897.
[6] U. Rabe, J. Janser, W. Arnold, Vibrations of free and surface-coupled atomic force microscope cantilevers: theory and experiment, *Review of Scientific Instruments* 67 (1996) 3281–3293.
[7] E. Kester, U. Rabe, L. Presmanes, P. Tailhades, W. Arnold, Measurement of Young's modulus of nanocrystalline ferrites with spinel structures by atomic force acoustic microscopy, *Journal of Physics and Chemistry of Solids* 61 (2000) 1275–1284.
[8] U. Rabe, S. Amelio, E. Kester, V. Scherer, S. Hirsekorn, W. Arnold, Quantitative determination of contact stiffness using atomic force acoustic microscopy, *Ultrasonics* 38 (2000) 430–437.
[9] M. Alexe, A. Gruverman, *Nanoscale Characterization of Ferroelectric Materials*, Springer, Berlin, 2004.
[10] S. Hong, *Nanoscale Phenomena in Ferroelectric Thin Films*, Kluwer Academic, Boston, 2003.
[11] C. Harnagea, A. Pignolet, M. Alexe, D. Hesse, Higher-order electromechanical response of thin films by contact resonance, *IEEE Transactions on Ultrasonics, Ferroelectrics, and Frequency Control* 53 (12) (2006) 2309–2322.
[12] A. Gruverman, S. Kalinin, Piezoresponse force microscopy and recent advances in nanoscale studies of ferroelectrics, *Journal of Materials Science* 41 (2006) 107–116.
[13] P. Guthner, K. Dransfeld, Local poling of ferroelectric polymers by scanning force microscopy, *Applied Physics Letters* 61 (1992) 1137–1139.
[14] A. Gruverman, H. Tokumoto, A.S. Prakash, S. Aggarwal, B. Yang, M. Wuttig, R. Ramesh, O. Auciello, Nanoscale imaging of domain dynamics and retention in ferroelectric thin film, *Applied Physics Letters* 71 (1997) 3492–3494.
[15] T. Hidaka, M. Maruyama, M. Saitoh, N. Mikoshiba, M. Shimizu, T. Shiosaki, L.A. Wills, R. Hiskes, S.A. Dicarolis, J. Amano, Formation and observation of 50 nm polarized domains in Pb $Zr_{1-x}Ti_xO_3$ thin films using scanning probe microscope, *Applied Physics Letters* 68 (1996) 2358–2359.
[16] F. Felten, G. Schneider, J. Saldana, S. Kalinin, Modeling and measurement of surface displacement in $BaTiO_3$ bulk material in piezoresponse force microscopy, *Journal of Applied Physics* 96 (1) (2004) 563–568.
[17] S. Hong, J. Woo, H. Shin, J. Joen, Y. Pak, E. Colla, N. Settar, E. Kim, K. No, Principle of ferroelectric domain imaging using atomic force microscopy, *Journal of Applied Physics* 89 (2) (2001) 1377–1386.
[18] S. Kalinin, B. Rodriguez, S. Jesse, K. Seal, R. Proksch, S. Hohlbauch, I. Revenko, G. Thompson, A. Vertegel, Towards local electromechanical probing of cellular and biomolecular systems in a liquid environment, *Nanotechnology* 18 (2007) 424020 (1–10).
[19] S. Kalinin, B. Rodriguez, S. Jesse, J. Shin, A. Baddorf, P. Gupta, H. Jain, D. Williams, A. Gruverman, Vector piezoresponse force microscopy, *Microscope and Microanalysis* 12 (2006) 206–220.
[20] C.A. Papadopoulos, A.D. Dimarogonas, Coupled longitudinal and bending vibrations of a rotating shaft with an open crack, *Journal of Sound and Vibration* 117 (1987) 81–93.
[21] C.A. Papadopoulos, A.D. Dimarogonas, Coupling of bending and torsional vibration of a cracked Timoshenko shaft, *Archive of Applied Mechanics* 57 (1987) 257–266.
[22] C.A. Papadopoulos, A.D. Dimarogonas, Coupled vibration of cracked shafts, *Journal of Vibration and Acoustics* 114 (1992) 461–467.
[23] A.C. Chasalevris, C.A. Papadopoulos, Coupled horizontal and vertical bending vibrations of a stationary shaft with two cracks, *Journal of Sound and Vibration* 309 (2008) 507–528.
[24] A.K. Darpe, K. Gupta, A. Chawla, Coupled bending, longitudinal and torsional vibrations of cracked rotor, *Journal of Sound and Vibration* 269 (2004) 33–60.
[25] E. Dokumaci, An exact solution for coupled bending and torsion vibration of uniform beams having single cross-sectional symmetry, *Journal of Sound and Vibration* 119 (1987) 443–449.
[26] R.E.D. Bishop, S.M. Cannon, S. Miao, On the coupled bending and torsional vibration of uniform beam, *Journal of Sound and Vibration* 131 (1989) 457–464.
[27] J.R. Banerjee, S. Guo, W.P. Howson, Exact dynamic stiffness matrix of a bending–torsion coupled beam including warping, *Computers and Structures* 59 (1996) 612–621.
[28] A.N. Bercin, M. Tanaka, Coupled flexural–torsional vibrations of Timoshenko beams, *Journal of Sound and Vibration* 207 (1997) 47–59.
[29] H. Gokdag, O. Kopmaz, Coupled bending and torsional vibrations of a beam with tip and in-span attachments, *Journal of Sound and Vibration* 287 (2005) 591–610.
[30] S.N. Mahmoodi, N. Jalili, Coupled flexural–torsional nonlinear vibrations of piezoelecrically-actuated microcantilevers with application to friction force microscopy, *ASME Journal of Vibration and Acoustics* 130 (6) (2008) 061003 (1–10).
[31] S. Kalinin, D. Bonnell, Imaging mechanism of piezoresponse force microscopy of ferroelectric surfaces, *Physical Review B* 65 (2002) 125408 (1–11).
[32] B.J. Rodriguez, S. Jesse, A.P. Baddorf, S. Kalinin, High resolution electromechanical imaging of ferroelectric materials in a liquid environment by piezoresponse force microscopy, *Physical Review letters* 96 (2006) 237602 (1–4).
[33] C.P. Green, J.E. Sader, Frequency response of cantilever beams immersed in viscous fluids near a solid surface with applications to the atomic force microscope, *Journal of Applied Physics* 98 (2005) 114913 (1–12).
[34] S. Basak, A. Raman, S.V. Garimella, Hydrodynamic loading of microcantilevers vibrating in viscous fluids, *Journal of Applied Physics* 99 (2006) 114906 (1–10).
[35] H. Hosakaa, K. Itaob, S. Kurodab, Damping characteristics of beam-shaped micro-oscillators, *Sensors and Actuators A: Physical* 49 (1995) 87–95.